Reactionless Path Planning Strategies for Capture of Tumbling Objects in Space Using a Dual-Arm Robotic System

Suril V. Shah[1]
Robotics Research Center, IIIT Hyderabad, Andhra Pradesh, 500032, India
[1]surilshah@iiit.ac.in

and

Inna Sharf[2] and Arun K. Misra[3]
Mechanical Engineering Department, McGill University, Montreal, QCH3A 0C3, Canada
[2]inna.sharf@mcgill.ca, [3]arun.misra@mcgill.ca

This paper presents strategies for point-to-point reactionless manipulation of a satellite mounted dual-arm robotic system for capture of tumbling orbiting objects, such as out-of-commission satellites and space debris. Use of the dual-arm robot could be more effective than the single arm when there is no provision for a grapple fixture or the object is tumbling. The dual arms can also provide dexterous manipulation. As the main objective in capture of orbital objects is to move the end-effector from initial position to the grapple point with desired velocity, the task-level reactionless constraints in terms of end-effector velocities are derived. The trajectory planned using these constraints, however, results in several singular points within the robot's workspace. In order to overcome this shortcoming, three point-to-point path planning strategies are presented, which improve the reactionless operation of the dual-arm robot. The strategies are illustrated by carrying out simulations for a 6-degree-of-freedom (DOF) dual-arm robotic system mounted on a satellite.

[1]corresponding author

I. Introduction

Autonomous on-orbit services, such as capture of orbiting objects, and refueling, repair and refurbishment of disabled satellites, using a robot mounted on a service satellite will be one of the important space operations in the future [1-3]. Particularly, active debris removal [3] has gained a lot of attention in the recent years due to the increase in the number of debris. While performing these on-orbit services, it is desirable that the fuel consumption to overcome any attitude disturbance of the base satellite is negligible, as limited fuel is mainly reserved for orbital transfer maneuvers. The main motivation behind capturing space debris is to avoid their possible collision with a working satellite in the same orbit. Some research efforts have been directed towards achieving capture of a satellite with zero attitude disturbances to the base. This is also commonly referred to as reactionless manipulation. Such reactionless manipulation of a robot mounted on a satellite can translate into fuel savings and increase the operating life of the servicing system.

In this regard, an optimization technique was proposed in [4] for minimization of the base reactions, which did not lead to a satisfactory result on reactionless manipulation. The concept of disturbance map was proposed in [5], which provided the minimum attitude disturbance paths leading to lower fuel consumption. Later, a more effective extended disturbance map was also proposed in [6]. These maps indeed help in reducing attitude disturbance, but may not lead to nil attitude disturbance. A unique design of manipulator was provided in [7] that led to reactionless manipulation. However, the major disadvantage of such a design is that it makes the robot architecture very complex. A reaction null space (RNS) based path planning was introduced in [8] for reactionless manipulation of a robot with flexible base. Later, in [9] the RNS based approach was used for control of space robots. It was shown in [8-9] that the joint velocities, obtained using the RNS formulation, result in zero reaction moments on the satellite-base. Subsequently, the flight validation with ETS-VII space robot and its extension to a kinematically redundant arm, for the zero reaction maneuvers, were presented in [10]. It was shown in [10] that the constraints for reactionless manipulation, in terms of joint velocities, can be augmented with the task-level constraints in order to obtain desired motion of the end-effector. The RNS-based concept was also used in [11] for capture of a tumbling satellite. Moreover, the RNS-based approach with backward integration was attempted in [12] for trajectory planning of 2-link robot in the approach phase. Reactionless motion of a space robot when capturing an unknown tumbling target was also presented in [13] based on the momentum conservation equation and the recursive least squares method.

In the above mentioned studies, the focus was mainly on completing the task with a single-arm robot. However, when the orbiting object does not have provision for grapple or is tumbling, the interception may be very difficult. In such cases, interception using a dual-arm robotic system can be appealing as this will increase the probability of grasp in comparison to a single-arm robot. Use of a dual-arm robot was described in [14], where one arm traced a given path while the second arm worked both to control the base attitude and to optimize the total operational torque of the system. The path planning of a planar dual-arm free-floating manipulator was also presented in [15]. In both [14] and [15], the second arm was only involved in attitude control of the base satellite rather than capture of the object. An autonomous approach for berthing of a moving satellite with two robots using a flexible wrist mechanism and impedance control was proposed in [16]. Capture of a spinning object by two flexible manipulators using hybrid position/force control and vibration suppression control was also presented in [17]. A hardware-in-the-loop simulation of the spatial dual-arm space robot was presented in [18]. In [16-18], the robot arms were manipulated without paying any attention to the base attitude. More recently, in [19], the coordinated motion planning of a spatial dual-arm space robot for target capture was presented. In that work also, capture of the target with both arms was carried out without regard to the base attitude.

It is worth noting that in the above cited works, either the dual arms capture the orbiting object regardless of the attitude of the base satellite or the one arm captures the object while the second arm is specifically used to control the attitude of the satellite. Thus, the reactionless capture using a dual-arm robotic system is least explored in the literature. The reactionless trajectories have to be designed such that the two arms start from different initial configurations and intercept the designated points on the object. It is also essential that both end-effectors capture the tumbling object with velocity equal to that of the contact points in order to avoid any significant impact. Hence, the major challenge in capture of a tumbling object is point-to-point reactionless manipulation of the robot arms with desired end-effector velocities at the capture instant. This is a complex problem as the reactionless constraints are nonholonomic and the resulting path has many singular points within the robot's workspace [10]. In comparison to the single-arm manipulation, the case of dual-arm manipulation requires that the paths have to be planned such that both arms stay away from singular configurations, which themselves are path dependents.

Motivated by these facts, the reactionless point-to-point path planning strategies are proposed in this work for dual-arm robotic systems for capture of a tumbling object. In the

present work, the two arms are moved so as to produce zero net reaction moment in order to capture the tumbling target. Compared to the single-arm scenario, reactionless manipulation of the dual-arm may bring forth some interesting aspects of path planning. The point-to-point motion is achieved by deriving the task-level reactionless constraints for dual-arm robotic system by projecting the joint-level reactionless constraints [8] using the Generalized Jacobian Matrix [20]. As the resulting equations are highly constrained and have many singular points within the robot's workspace, three point-to-point path planning strategies are also presented. Extension of reactionless path planning to a dual-arm robotic system and strategies to avoid singular configurations are the main contributions of this work. Numerical illustrations are provided using a 6-DOF dual-arm robotic system.

The rest of the paper is organized as follows: Some mathematical preliminaries are provided in Section II. The reactionless manipulation of the dual-arm robotic system is presented in Section III, whereas several point-to-point reactionless path planning strategies are developed in Section IV. Finally, conclusions are given in Section V.

II. Preliminaries and Notation

In this section the equations of motion for dual-arm robotic systems and constraints for reactionless manipulation are derived as an extension of those given in [10] for a single-arm robotic system.

A. Equations of motion

The equations of motion for an n-DOF robot mounted on a floating-base can be written similarly to those in [10] as:

$$\begin{bmatrix} \mathbf{H}_b & \mathbf{H}_{bm} \\ \mathbf{H}_{bm}^T & \mathbf{H}_m \end{bmatrix} \begin{bmatrix} \ddot{\mathbf{x}}_b \\ \ddot{\boldsymbol{\varphi}} \end{bmatrix} + \begin{bmatrix} \mathbf{c}_b \\ \mathbf{c}_m \end{bmatrix} = \begin{bmatrix} \mathbf{F}_b \\ \boldsymbol{\tau}_m \end{bmatrix} + \begin{bmatrix} \mathbf{J}_b^T \\ \mathbf{J}_m^T \end{bmatrix} \mathbf{F}_h \tag{1}$$

where $\mathbf{H}_b \in \mathrm{R}^{6\times 6}$ and $\mathbf{H}_m \in \mathrm{R}^{n\times n}$ are the inertia matrices of the base and manipulator, respectively, $\mathbf{H}_{bm} \in \mathrm{R}^{6\times n}$ is the coupling inertia matrix, $\ddot{\mathbf{x}}_b \in \mathrm{R}^6$ is the vector of linear and angular accelerations of the base, $\ddot{\boldsymbol{\varphi}} \in \mathrm{R}^n$ is the vector of joint accelerations, $\mathbf{c}_b \in \mathrm{R}^6$ and $\mathbf{c}_m \in \mathrm{R}^n$ are the velocity dependent nonlinear terms of the base and manipulator, $\mathbf{F}_b$ and $\mathbf{F}_h \in \mathrm{R}^6$ are the vectors of force and moment exerted on the centroid of the base and end-effector, respectively, $\boldsymbol{\tau}_m \in \mathrm{R}^n$ is the manipulator joint torque, $\mathbf{J}_b \in \mathrm{R}^{6\times 6}$ and $\mathbf{J}_m \in \mathrm{R}^{6\times n}$ are the Jacobian

matrices for the base and manipulator. For the dual-arm robotic system, $\mathbf{H}_{bm}$, $\mathbf{H}_m$, $\dot{\boldsymbol{\varphi}}$, $\mathbf{c}_m$, $\boldsymbol{\tau}_m$, $\mathbf{J}_b$, $\mathbf{J}_m$ and $\mathbf{F}_h$ can be written as follows:

$$\mathbf{H}_{bm} = \begin{bmatrix} \mathbf{H}_{bm1} & \mathbf{H}_{bm2} \end{bmatrix},\ \mathbf{H}_m = \begin{bmatrix} \mathbf{H}_{m1} & \mathbf{O} \\ \mathbf{O} & \mathbf{H}_{m2} \end{bmatrix},\ \ddot{\boldsymbol{\varphi}} = \begin{bmatrix} \ddot{\boldsymbol{\varphi}}_{m1} \\ \ddot{\boldsymbol{\varphi}}_{m2} \end{bmatrix}, \mathbf{c}_m = \begin{bmatrix} \mathbf{c}_{m1} \\ \mathbf{c}_{m2} \end{bmatrix},$$
$$\boldsymbol{\tau}_m = \begin{bmatrix} \boldsymbol{\tau}_{m1} \\ \boldsymbol{\tau}_{m2} \end{bmatrix}, \mathbf{J}_b = \begin{bmatrix} \mathbf{J}_{b1} \\ \mathbf{J}_{b2} \end{bmatrix}, \mathbf{J}_m = \begin{bmatrix} \mathbf{J}_{m1} & \mathbf{O} \\ \mathbf{O} & \mathbf{J}_{m2} \end{bmatrix} \text{ and } \mathbf{F}_h = \begin{bmatrix} \mathbf{F}_{h1} \\ \mathbf{F}_{h2} \end{bmatrix} \tag{2a}$$

where the subscripts 1 and 2 represent arm-1 and arm-2, respectively. The floating-base module of the *Recursive Dynamics Simulator* (*ReDySim*) [21], developed based on (1-2), is used for the simulations carried out in this paper.

B. Constraints for reactionless manipulation

The matrices $\mathbf{H}_b$ and $\mathbf{H}_{bm}$, of (1), may also be expressed as

$$\mathbf{H}_b = \begin{bmatrix} \mathbf{H}_{b\_v} & \mathbf{H}_{b\_c}^T \\ \mathbf{H}_{b\_c} & \mathbf{H}_{b\_\omega} \end{bmatrix} \text{ and } \mathbf{H}_{bm} = \begin{bmatrix} \mathbf{H}_{bm\_v} \\ \mathbf{H}_{bm\_\omega} \end{bmatrix} \tag{3a}$$

Now, the constraints for reactionless manipulation can be written using those in [10] as

$$\tilde{\mathbf{H}}_{bm}\dot{\boldsymbol{\varphi}} = 0 \text{ where } \tilde{\mathbf{H}}_{bm} = \mathbf{H}_{bm\_\omega} - \mathbf{H}_{b\_v}^{-1}\mathbf{H}_{b\_c}\mathbf{H}_{bm\_v} \tag{3b}$$

Equation (3b) represents the nonholonomic constraints, where $\dot{\boldsymbol{\varphi}}$ belongs to the subspace of reactionless motion of the robot. The above equation forms the constraint leading to zero reaction moments but non-zero reaction forces. It is assumed that the satellite has reaction jets or thrusters to take care of the base reaction forces. As in the previous literature, hereafter, the term *reactionless manipulation* will imply manipulation with zero base moments only. For the dual-arm robotic system, (3b) can also be expressed as

$$\begin{bmatrix} \tilde{\mathbf{H}}_{bm1} & \tilde{\mathbf{H}}_{bm2} \end{bmatrix} \begin{bmatrix} \dot{\boldsymbol{\varphi}}_{m1} \\ \dot{\boldsymbol{\varphi}}_{m2} \end{bmatrix} = 0 \text{ or } \tilde{\mathbf{H}}_{bm1}\dot{\boldsymbol{\varphi}}_{m1} + \tilde{\mathbf{H}}_{bm2}\dot{\boldsymbol{\varphi}}_{m2} = 0 \tag{4}$$

It can be seen from (4) that for the dual-arm robot the sum of the coupling angular momenta of both arms, not of the individual, has to be zero. Solution of (4) for $\dot{\boldsymbol{\varphi}}_{m1}$ and $\dot{\boldsymbol{\varphi}}_{m2}$ can be obtained using the pseudo inverse approach [8]. It is noted that (3b-4) represent the constraints as a function of joint velocities, and will be referred to as joint-level reactionless constraints.

III. Reactionless Manipulation of Dual-Arm Robot

In this section, the task-level constraints for reactionless manipulation are obtained first, followed by a numerical example and discussion on singularity.

A. Task-level constraints for reactionless manipulation

Since (4) is represented in terms of joint velocities, it cannot readily provide a solution for the reactionless motion of the end-effectors in the Cartesian space. In such cases, one may use the constraint augmentation technique proposed in [10] for a single-arm robotic system. In the present work the point-to-point path planning for the end-effectors of the dual-arm robot is carried out using task-level reactionless constraints. These constraints are obtained by projecting the constraints in (4) using the Generalized Jacobian Matrix (GJM) [20]. For the dual-arm robot, the end-effectors' velocities are related to joint velocities by

$$\dot{\mathbf{x}}_{h1} = \mathbf{J}_{g1}\dot{\boldsymbol{\varphi}}_{m1} + \mathbf{J}_{g12}\dot{\boldsymbol{\varphi}}_{m2}, \text{ where } \mathbf{J}_{g1} = \mathbf{J}_{m1} - \mathbf{J}_{b1}\mathbf{H}_b^{-1}\mathbf{H}_{bm1} \text{ and } \mathbf{J}_{g12} = \mathbf{J}_{b1}\mathbf{H}_b^{-1}\mathbf{H}_{bm2} \tag{5}$$

$$\dot{\mathbf{x}}_{h2} = \mathbf{J}_{g2}\dot{\boldsymbol{\varphi}}_{m2} + \mathbf{J}_{g21}\dot{\boldsymbol{\varphi}}_{m1}, \text{ where } \mathbf{J}_{g2} = \mathbf{J}_{m2} - \mathbf{J}_{b2}\mathbf{H}_b^{-1}\mathbf{H}_{bm2} \text{ and } \mathbf{J}_{g21} = \mathbf{J}_{b2}\mathbf{H}_b^{-1}\mathbf{H}_{bm1} \tag{6}$$

where $\mathbf{J}_{g1}$ and $\mathbf{J}_{g2}$ are the Generalized Jacobian matrices of the individual arms 1 and 2, respectively, and $\mathbf{J}_{g12}$ and $\mathbf{J}_{g21}$ are the coupling Jacobians. The task-level constraints are obtained by substituting expressions for $\ddot{\boldsymbol{\varphi}}_{m1}$ and $\ddot{\boldsymbol{\varphi}}_{m2}$ from (5-6) into (4) as:

$$\begin{bmatrix}\tilde{\mathbf{H}}_{bh1} & \tilde{\mathbf{H}}_{bh2}\end{bmatrix}\begin{bmatrix}\dot{\mathbf{x}}_{h1}\\ \dot{\mathbf{x}}_{h2}\end{bmatrix} = 0 \text{ or } \tilde{\mathbf{H}}_{bh1}\dot{\mathbf{x}}_{h1} + \tilde{\mathbf{H}}_{bh2}\dot{\mathbf{x}}_{h2} = 0 \tag{7}$$

In the above,

$$\begin{bmatrix}\tilde{\mathbf{H}}_{bh1} & \tilde{\mathbf{H}}_{bh2}\end{bmatrix} = \begin{bmatrix}\tilde{\mathbf{H}}_{bm1} & \tilde{\mathbf{H}}_{bm2}\end{bmatrix}\mathbf{J}_g^{-1} \text{ and } \mathbf{J}_g = \begin{bmatrix}\mathbf{J}_{g1} & \mathbf{J}_{g12}\\ \mathbf{J}_{g21} & \mathbf{J}_{g2}\end{bmatrix} \tag{8}$$

where $\mathbf{J}_g$ may be interpreted as GJM of the dual-arm system. We assume that $\mathbf{J}_g$ is invertible; a pseudo inverse can be used otherwise.

Equation (7) represents the task-level reactionless constraints and will be used for point-to-point reactionless manipulation of the dual-arm robot. The degree-of-redundancy (DOR), f_r, associated with (7) is given by the difference in the number of columns and rows of $\begin{bmatrix}\tilde{\mathbf{H}}_{bh1} & \tilde{\mathbf{H}}_{bh2}\end{bmatrix}$. Solution of (7) belongs to the f_r-dimensional subspace of R^n. In other words, f_r end-effectors' velocities, out of $\dot{\mathbf{x}}_{h1}$ and $\dot{\mathbf{x}}_{h2}$, can be controlled or prescribed independently. Solution of (7) can be obtained using the pseudo inverse approach as:

$$\dot{\mathbf{x}}_h = (\mathbf{E} - \tilde{\mathbf{H}}_{bh}^{+}\tilde{\mathbf{H}}_{bh})\dot{\boldsymbol{\xi}} \tag{9}$$

where $\dot{\mathbf{x}}_h = [\dot{\mathbf{x}}_{h1}^T \quad \dot{\mathbf{x}}_{h2}^T]^T$, $\tilde{\mathbf{H}}_{bh} = [\tilde{\mathbf{H}}_{bh1} \quad \tilde{\mathbf{H}}_{bh2}]$, $(\mathbf{E} - \tilde{\mathbf{H}}_{bh}^{+}\tilde{\mathbf{H}}_{bh})$ is the null-space projector and $\dot{\boldsymbol{\xi}}$ is an arbitrary velocity vector mapped into the null space. Alternatively, one may use co-ordinate partitioning as:

$$\begin{bmatrix} \tilde{\mathbf{H}}_{bh}^{d} & \tilde{\mathbf{H}}_{bh}^{i} \end{bmatrix} \begin{bmatrix} \dot{\mathbf{x}}_h^d \\ \dot{\mathbf{x}}_h^i \end{bmatrix} = 0 \tag{10}$$

where $\dot{\mathbf{x}}_h^i$ and $\dot{\mathbf{x}}_h^d$ are the independent or free and dependent velocities. In (10), the number of independent velocities is equal to f_r, whereas the dependent velocities are obtained as

$$\dot{\mathbf{x}}_h^d = -\tilde{\mathbf{H}}_{bh}^{d\,-1}\tilde{\mathbf{H}}_{bh}^{i}\dot{\mathbf{x}}_h^i \tag{11}$$

Equations (10-11) are preferred over (9), as the former allow one to directly prescribe f_r end-effector velocities independently. For example, for the 6-link planar dual-arm robot, shown in Fig. 1, the linear and angular velocities of the end-effectors of arm-1, i.e., (v_{E1x}, v_{E1y}, ω_{E1}), and arm-2, i.e., (v_{E2x}, v_{E2y}, ω_{E2}), are the six variables in the task-space. The DOR associated with (7) is five, and hence, any five out of the above six can be chosen independently. On the other hand, solution of (11) can be obtained, provided $\tilde{\mathbf{H}}_{bh}^{d}$ is invertible. Otherwise, (11) will lead to a singularity as illustrated in section III-C.

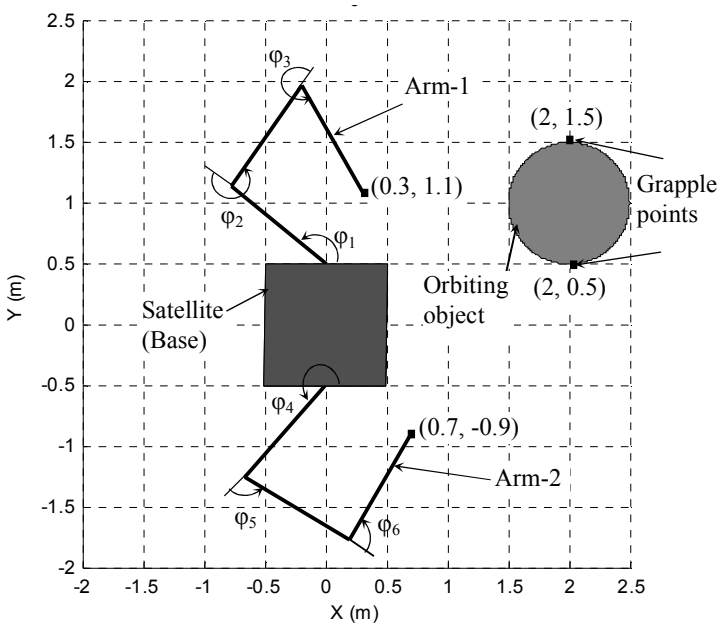

Figure 1. A dual-arm robotic system mounted on a satellite

B. A numerical example

In order to illustrate the use of (10-11), a planar dual-arm robotic system mounted on a satellite, as shown in Fig. 1, is considered. Each arm is comprised of three rigid links and 3-DOF. The centers-of-mass of the satellite and orbiting object lie at (0 m, 0 m), and (2 m, 1m), respectively. The dual arms are initially in a non-symmetric configuration, as in practice it is not possible to achieve perfect symmetry. The points to be grappled on the object are also shown in Fig. 1. For this particular example, the object is assumed to be stationary relative to satellite. The geometric and inertia properties of the dual arms and satellite are given in Table I.

TABLE I. MODEL PARAMETERS OF THE DUAL-ARM AND SATELLITE

	Satellite	Arm 1			Arm 2			Orbital
	(0)	1	2	3	4	5	6	object
Mass (Kg)	500	10	10	10	10	10	10	-
Length (m)	1×1	1	1	1	1	1	1	1m dia.
I_{zz}(Kg.m^2)	83.61	1.05	1.05	1.05	1.05	1.05	1.05	-

Equations (10-11) are used to obtain the reactionless motion in the Cartesian space. As the dual-arm robot has DOR equal to five, the five velocities, v_{E1x}, v_{E1y}, v_{E2x}, v_{E2y} and ω_{E2}, are chosen as free or independent, i.e., $\dot{\mathbf{x}}_h^i$, while ω_{E1} is chosen as the dependent velocity, i.e., $\dot{\mathbf{x}}_h^d$. The independent velocities are designed using a fourth order interpolating polynomial as follows:

$$\dot{x}(t) = \left[a + b\left(\frac{t}{T}\right)^2 + 4c\left(\frac{t}{T}\right)^3 + 5d\left(\frac{t}{T}\right)^4 \right] \tag{12}$$

where $a = \dot{x}_I$, $b = 10e - (6\dot{x}_I + 4\dot{x}_F)$, $c = -15e + (8\dot{x}_I + 7\dot{x}_F)$, $d = 6e - (3\dot{x}_I + 3\dot{x}_F)$, and $e = [x_F - x_I]/T$. Moreover, (x_I and x_F) and ($\dot{x}_I$ and $\dot{x}_F$) are the initial and final positions and velocities, respectively. Equation (12) ensures zero initial and final acceleration. The initial and final positions are summarized in Table II, while the initial velocities of the end-effectors are assumed to be zero. In order to avoid high impact forces, the final velocities are set to match those of the grapple points, which are zeros in this particular example. With the above, the dependent velocity leading to reactionless manipulation is obtained using (11).

TABLE II. INITIAL AND FINAL CONFIGURATIONS OF THE DUAL-ARM

	p_{E1x}(m)	p_{E1y} (m)	p_{E2x}(m)	p_{E2y} (m)	φ_{E2} (rad)
t = 0s	0.3	1.1	0.7	-0.9	1.0472
T = 120s	2	1.5	2	0.5	1.0472

Note: Initial orientation of the end-effector was taken as taken as –1.0472 rad

Simulation of the dual-arm robotic system moving to the grapple points on the orbiting object was carried out for the time period of 120 sec. The torque inputs following Proportional and Derivative (PD) control law given by (13) were used for carrying out the dynamic simulations:

$$\boldsymbol{\tau}_{mk} = \mathbf{K}_p(\boldsymbol{\varphi}_{dk} - \boldsymbol{\varphi}_{ak}) + \mathbf{K}_d(\dot{\boldsymbol{\varphi}}_{dk} - \dot{\boldsymbol{\varphi}}_{ak}), \quad k = 1, 2 \tag{13}$$

In (13), $\mathbf{K}_p$ and $\mathbf{K}_d$ are the diagonal matrices of proportional and derivative gains, and $\dot{\boldsymbol{\varphi}}_{dk}$ and $\dot{\boldsymbol{\varphi}}_{ak}$ are the vectors of desired and actual joint rates, respectively, of the k^{th} arm. The vector $\dot{\boldsymbol{\varphi}}_{dk}$ is obtained using (5-6) from already designed end-effectors' velocities in (10-12). The diagonal elements of $\mathbf{K}_p$ and $\mathbf{K}_d$ are obtained empirically and are assumed here to be 49 and 16, respectively. The inverse dynamics control for contacting robot, as proposed in [22-23], can also be used, however, (13) is used here as dual-arm in approach phase is not subjected to any external constraints.

The paths travelled by the end-effectors are shown in Fig. 2 by the dotted curves. Figure 2 also shows the final configuration of the dual-arm where the final positions of the end-effectors match with those provided in Table II. The angular velocity of the base, as depicted in Fig. 3, is of $O(10^{-6})$, proving reactionless manipulation of the dual-arm. Moreover, the final velocities of both end-effectors are zero as shown in Fig. 4. To provide partial validation of the results obtained using the ReDySim, the linear and angular momenta are also plotted in Fig. 5. The change in linear and angular momenta is of $O(10^{-7})$, confirming conservation of momenta by the dynamics simulator.

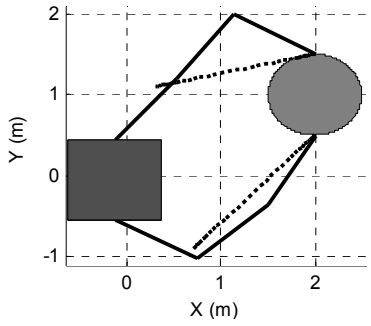

Figure 2. Motion in X-Y plane

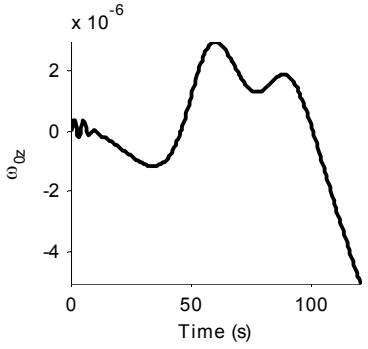

Figure 3. Angular velocity of base

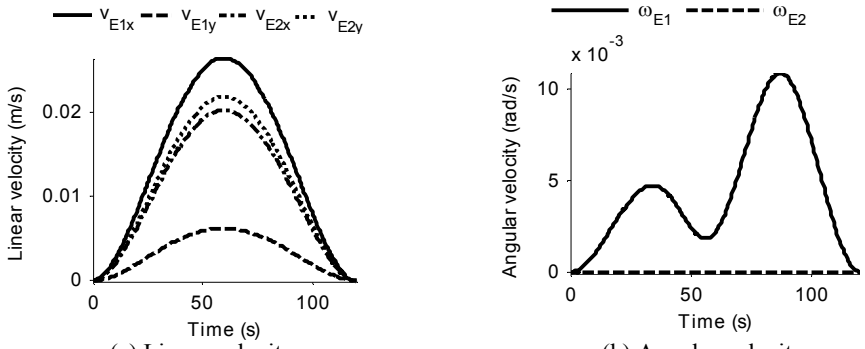

(a) Linear velocity (b) Angular velocity

Figure 4. Velocity of the end-effectors of the dual-arm

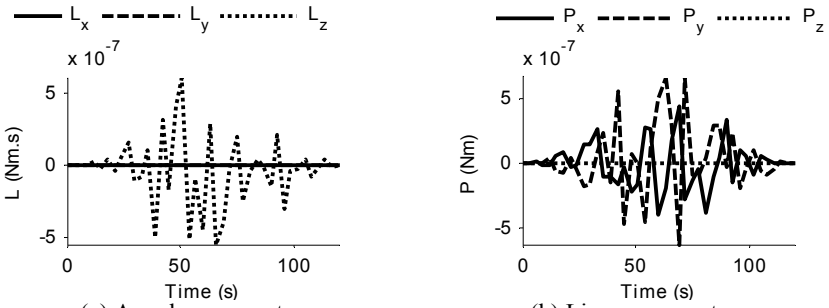

(a) Angular momentum (b) Linear momentum

Figure 5. Angular and linear momenta

C. Illustration of singularity

Equation (11) is highly constrained and the resulting path can have many singular points within the robot's workspace. It is worth noting that these singular points are in general different from those associated with dynamic singularities [24] and occur when the configuration dependent matrix $\tilde{\mathbf{H}}_{bh}^{d}$, employed in (11), becomes non-invertible. Therefore, it is important to detect this singularity so that appropriate corrective action can be taken.

It is interesting to observe that the point-to-point path planned using (10-11) can be non-singular for one set of desired final velocities and singular for another set. This is due to the nonholonomic nature of the path planner. We illustrate this by attempting to find a solution for the same example as considered before, but with the object now spinning at constant angular rate of 0.02 rad/s, resulting in the velocities of the two grapple points of -0.01 and 0.01 m/s in the X-direction. In this scenario, the path planner and simulation failed at t=62.1 sec, because of the singularity associated with $\tilde{\mathbf{H}}_{bh}^{d}$. Figure 6 plots the commonly used measure of matrix singularity defined as:

$$S = \sqrt{\det\left(\tilde{\mathbf{H}}_{bh}^{d}\tilde{\mathbf{H}}_{bh}^{d\,T}\right)} \tag{14}$$

while Fig. 7 shows that the torque at joint 3 is increasing rapidly as the singularity is nearing. Given that it is not possible to ensure a non-singular path with the planner defined by (11), we next propose alternative point-to-point strategies which can avoid such singular configurations while capturing a tumbling object.

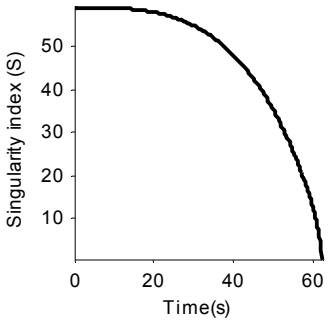

Figure 6. Singularity index

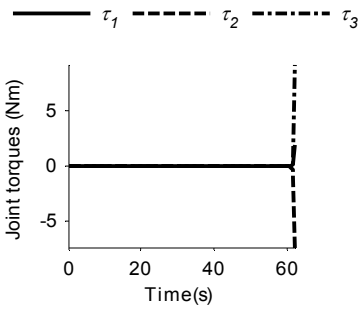

Figure 7. Joint torques of arm-1

IV. Point-to-Point Reactionless Path Planning Strategies

In this section three strategies are presented to alleviate the singularity problem in achieving reactionless manipulation of the dual-arm robotic system for capture of the tumbling object.

A. Reactionless manipulation through choice of independent variables

For the example considered in III-C, the number of independent variables used in the path planner was chosen equal to DOR, i.e., 5. As objective in point-to-point path planning is mainly to capture the tumbling object at grapple points with desired velocity, one may alternatively choose only the translational task-level velocities v_{E1x}, v_{E1y}, v_{E2x} and v_{E2y} as the independent variables, leaving ω_{E1} and ω_{E2} to be the dependent variables. The compromise on the trajectory of ω_{E1} makes (11) redundant and provides enhanced workspace. This is acceptable if the orientation of the end-effectors falls within the allowable limit at the time of capture. Therefore, the dependent velocities are calculated as:

$$\dot{\mathbf{x}}_h^d = -\tilde{\mathbf{H}}_{bh}^{d\,+}\tilde{\mathbf{H}}_{bh}^{i}\dot{\mathbf{x}}_h^i + (\mathbf{E} - \tilde{\mathbf{H}}_{bh}^{d\,+}\tilde{\mathbf{H}}_{bh}^{d})\dot{\boldsymbol{\xi}} \tag{15}$$

The example considered in III-C is now simulated by computing the dependent velocities according to (15) with $\dot{\boldsymbol{\xi}} = \mathbf{0}$. The resulting plots are illustrated in Figs. 8 and 9 and show that the end-effectors are able to reach the points on the spinning object with the required

velocities. The angular velocity of base is also shown in Fig. 10, which is of $O(10^{-6})$ confirming reactionless manipulation of the dual-arm. However, the path travelled by arm-1 traverses the object as shown in Fig. 11, which in a real setting would result in collision. In such situations, one may chose alternative value of $\dot{\xi}$. Another possible solution is to move the dual-arm to an intermediate point before it captures the object, as described in the following section.

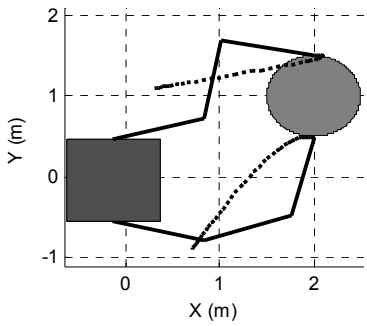

Figure 8. Motion in X-Y plane

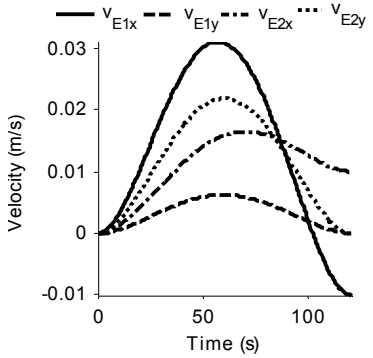

Figure 9. End-effector's velocity

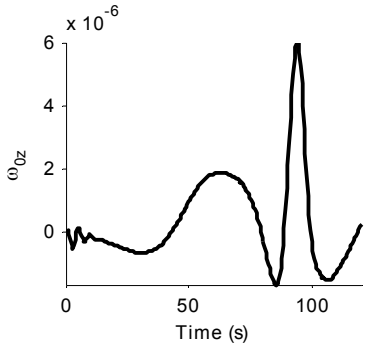

Figure 10. Angular velocity of base

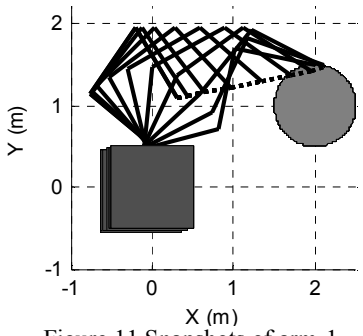

Figure 11.Snapshots of arm-1

B. Reactionless manipulation through intermediate points

In this approach, the intermediate points between initial and final points are considered when the end-effectors are not able to reach the grapple points according to (15) due to either singular configuration or collision. Then, we propose that the motion is planned as follows:

$$\dot{\mathbf{x}}_{hj}^{d} = -\tilde{\mathbf{H}}_{bh}^{d\,+}\tilde{\mathbf{H}}_{bh}^{i}\dot{\mathbf{x}}_{hj}^{i} + (\mathbf{E} - \tilde{\mathbf{H}}_{bh}^{d\,+}\tilde{\mathbf{H}}_{bh}^{d})\dot{\boldsymbol{\xi}}_{j}, \quad j = 1,..., p+1 \tag{16}$$

where $\dot{\mathbf{x}}_{hj}^{d}$ and $\dot{\mathbf{x}}_{hj}^{i}$ are the dependent and desired independent velocities from $(j\text{-}1)^{\text{th}}$ to j^{th} point, and p is total number of intermediate points. It may be noted that $\dot{\mathbf{x}}_{hj}^{i}$ are designed using (12), which allows one to prescribe initial and final velocities for each intermediate segment.

Equation (16) enables moving from the initial to intermediate point and intermediate to next point in a reactionless manner.

The procedure for the proposed "piecewise" path planner is illustrated by simulating the example of IV-A, however, with the end effectors of arm-1 and -2 commanded to travel via intermediate points (1.2, 1.8) and (1.5, -0.3), respectively. Moreover, the end-effector velocities of the two arms in the X-direction are gradually increased through values of -0.008m/s and 0.008 m/s at the intermediate points. Figures 12 and 13 show the simulation results, which depict that the end-effectors are able to reach the points on the spinning object with the required velocity. The dual-arm is able to move in a reactionless manner as the change in angular velocity of base is of $O(10^{-5})$ as shown in Fig. 14. The upper arm (arm-1) is also able to avoid a collision, as depicted in Fig.15. For collision avoidance a method based on repulsion potential field [25] can also be applied, which however is beyond the scope of the paper.

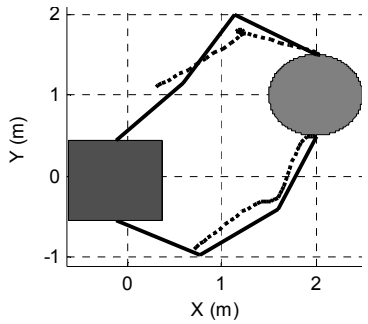

Figure 12. Motion in X-Y plane

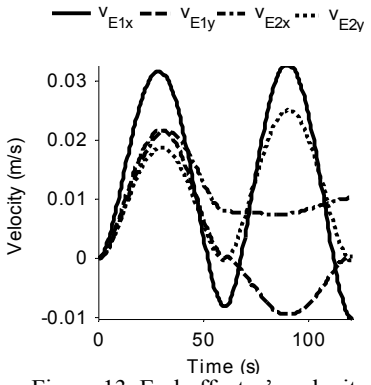

Figure 13. End-effector's velocity

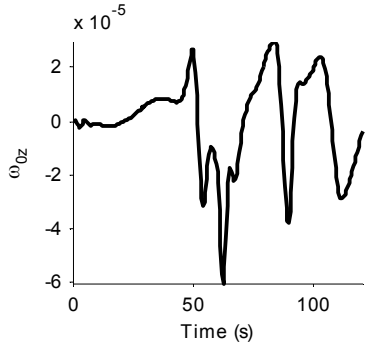

Figure 14. Angular velocity of base

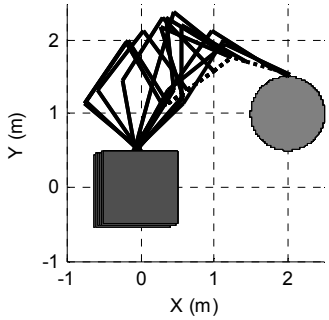

Figure 15. Snapshots of arm-1

It can be observed from Fig. 15 that the joint angle φ_2 (defined in Fig. 1) of arm-1traverses through a value φ_2=180, which corresponds to a dynamic singularity. Additional insight is

gleaned by considering, singularity indices for $\tilde{\mathbf{H}}_{bh}^{d}$ and $\mathbf{J}_{g1}$ (the GJM of arm-1) plotted in Figs. 16 and 17, respectively. It is seen that the peaks in Fig. 16 correspond to singular points in Fig. 17. Such situations are not desirable as they can result in high joint torque requirements. Even though for the problem under study, the joint torques shown in Fig. 18 remained in a reasonable range, high joint torques were observed when different intermediate points were chosen. The concept of hybrid manipulation is proposed next, which is found to be more advantageous when such dynamic singularities are unavoidable.

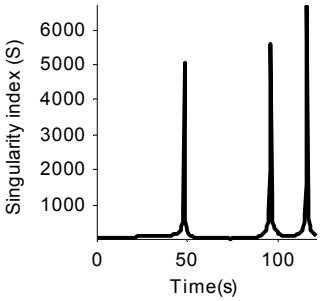

Figure 16. Singularity index S($\tilde{\mathbf{H}}_{bh}^{d}$)

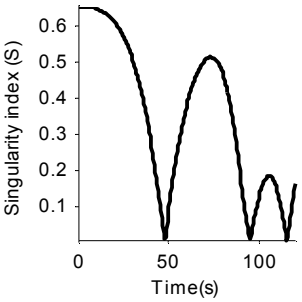

Figure 17. Singularity index S($\mathbf{J}_{g1}$)

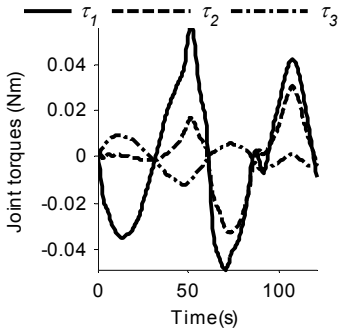

Figure 18.Joint torques for arm-1

C. Hybrid reactionless manipulation

In this approach, the path planning is carried out using both joint- and task-level constraints for reactionless manipulation, derived in (4) and (7), respectively. The joint-level constraints are mainly used to cross the singular configurations, whereas the task-level constraints are used to reach the desired points. Equation (15) is used for the task-level path planning, and the joint-level path planning is carried out similarly to (15) as

$$\dot{\boldsymbol{\varphi}}_h^d = -\tilde{\mathbf{H}}_{bm}^{d\,+}\tilde{\mathbf{H}}_{bm}^{i}\dot{\boldsymbol{\varphi}}_h^i + (\mathbf{E} - \tilde{\mathbf{H}}_{bm}^{d\,+}\tilde{\mathbf{H}}_{bm}^{d})\dot{\boldsymbol{\xi}} \tag{17}$$

In (17), $\tilde{\mathbf{H}}_{bm}^{d}$ is not function of the GJM, and hence, (17) is unaffected by dynamic singularity. The concept of hybrid reactionless manipulation is illustrated using the example solved in IV-B, however, with the motion of the dual–arm robot divided into three stages. In stage 1, the end-effectors travel form initial points to the intermediate points, illustrated in Table III, using the task-level planner of Eq. (15) The intermediate points are selected closer to the object such that that $\varphi_2 \neq 0$ or 180. Note that the angle φ_2 was -1.0472 rad in the beginning and -0.5331 rad at the end of stage 1. In stage2, the angle φ_2 is brought from -0.5331 to 0.5331 rad using joint-level planner of Eq. (17). In the third and final stage, the end-effectors travel from current to final position using task-level planner.

TABLE III. INITIAL AND FINAL CONFIGURATOIN FOR THE VARIOUS STAGES IN HYBRID MANIPULATION

		p_{E1x}(m)	p_{E1y} (m)	p_{E2x}(m)	p_{E2y} (m)	
Stage 1	t=0	0.3	1.1	0.7	-0.9	
	t=40	1.4	1.4	1.5	0.0	
		φ_2 (rad)	φ_4 (rad)	φ_4 (rad)	φ_5 (rad)	φ_6 (rad)
Stage 2	t=40[1]	-0.5331	-1.7383	-2.7462	1.7248	0.6594
	t=80	0.5331	-1.7383	-2.7462	1.7248	0.6594
		p_{E1x}(m)	p_{E1y} (m)	p_{E2x}(m)	p_{E2y} (m)	
Stage 3	t=80[2]	1.5761	1.9794	1.4942	-0.0035	
	T=120	2	1.5	2	0.5	

Note: 1. Joint angles correspond to the end-effector's position at the end of stage 1
2. End-effector's position correspond to the joint angles at the end of stage 2

Figure 19 shows that the end-effectors are able to reach the points on the spinning object. The end-effectors are also able to match the velocities of grapple points as depicted in Fig. 20. Figure 21 depicts that the angular velocity of the base is of $O(10^{-5})$, which ensure reactionless manipulation of the dual-arm. The singularity index for stages 1-3 is plotted in Fig. 22, which illustrate that $\tilde{\mathbf{H}}_{bh}^{d}$ is non-singular in stages 1 and 3, whereas $\tilde{\mathbf{H}}_{bm}^{d}$ is non-singular in stage 2. This shows the effectiveness of the hybrid reactionless manipulation.

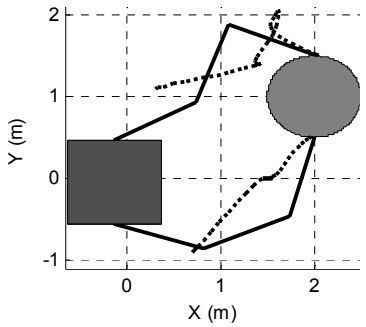

Figure 19. Motion in X-Y plane

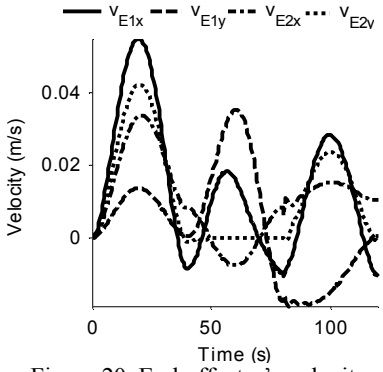

Figure 20. End-effector's velocity

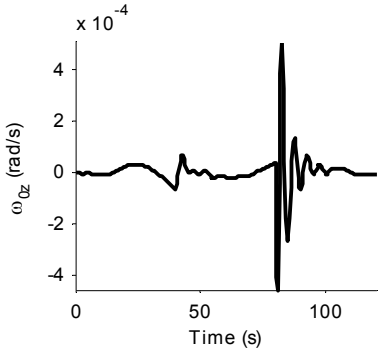

Figure 21. Angular velocity of base

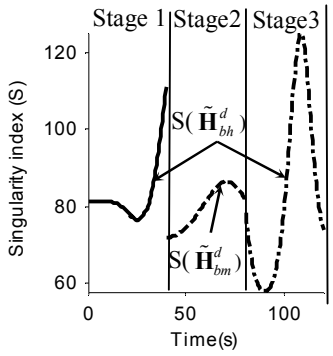

Figure 22. Singularity index

V. Conclusions

The point-to-point reactionless path planning for interception of the orbiting object using a dual-arm robotic system has been presented. It is shown that the reactionless paths contain singular points in the transformation between independent and dependent task velocities. To remedy this problem, three strategies, namely, through a choice of fewer than maximum independent variables, reactionless manipulation through intermediate points and hybrid reactionless manipulation, have been presented. By changing a subset of independent variables one can exploit the redundancy in the dual-arm robot to enhance the reactionless manipulation. On the other hand, reactionless manipulation through intermediate points allows one to obtain an alternative non-singular or collision-free path, whereas the hybrid reactionless manipulation helps in overcoming the dynamic singularity, which cannot be completely avoided using the former two approaches. The above three path planning strategies are simple yet effective for capturing the tumbling target using a dual-arm system in a reactionless manner.

Even though the above methods allow to move the dual-arm in a reactionless manner, the following issues need to be addressed: 1) development of a systematic approach for selection of the number of intermediate points and their locations, 2) calculation of optimum path out of the multiple reactionless paths resulting out of the point-to-point strategies, e.g., the path giving favourable orientation of the end-effector or minimum energy consumption, 3) use of inverse dynamics control for trajectory planning. These will be carried out as future work.

References

[1] F. Sellmaier, T. Boge, J. Spurmann, S. Gully, T. Rupp and F. Huber, "On-Orbit Servicing Missions: Challenges and Solutions for Spacecraft Operations," *AIAA SpaceOps Conference*, 2010, pp. 25-30.

[2] "On-Orbit Satellite Servicing Study," *NASA Project Report*, 2010 (http://ssco.gsfc.nasa.gov/servicing_study.html)

[3] J. Liou, "An active debris removal parametric study for LEO environment remediation," *Advances in Space Research, 47*(11), 1865-1876, 2011.

[4] C. L. Chung, S. Desa, and C. W. deSilva, "Base reaction optimization of redundant manipulators for space applications," *The Robotic Institute CMU-RI-TR*, pp. 88-17, 1988.

[5] S. Dubowsky, and M. A. Torres, "Path planning for space manipulators to minimize spacecraft attitude disturbances," *IEEE International Conference on Robotics and Automation*, 1991, pp. 2522-2528.

[6] M. A. Torres and S. Dubowsky, "Minimizing spacecraft attitude disturbances in space manipulator systems," *Journal of Guidance, Control, and Dynamics*, vol. 15, no. 4, pp. 1010-1017, 1992.

[7] E. Papadopoulos, and A. Abu-Abed, "Design and motion planning for a zero-reaction manipulator," *IEEE International Conference on Robotics and Automation*, 1994,pp. 1554-1559.

[8] D. N. Nenchev, K. Yoshida, and M. Uchiyama, "Reaction null-space based control of flexible structure mounted manipulating systems," *IEEE CDC*, 1996, Kobe, Japan, pp. 4118-4123.

[9] D. N. Nenchev and K. Yoshida, "Impact analysis and post-impact motion control issues of a free-floating space robot subject to a force impulse," *IEEE Transactions on Robotics and Automation*, vol. 15, no. 3, pp. 548-557, 1999.

[10]K. Yoshida, K. Hashizume and S. Abiko, "Zero reaction maneuver: Flight validation with ETS-VII space robot and extension to kinematically redundant arm," *IEEE International Conference on Robotics and Automation*, 2001, pp. 441-446.

[11]K. Yoshida, D. Dimitrov and H. Nakanishi, "On the capture of tumbling satellite by a space robot," *IEEE International Conference on Intelligent Robots and Systems*, 2006, pp. 4127-4132.

[12]P. Piersigilli, I. Sharfand A. K. Misra, "Reactionless capture of a satellite by a two degree-of-freedom manipulator," *Acta Astronautica*, vol. 66, no. (1-2), pp. 183-192, 2010.

[13]T. Nguyen-Huynh and I. Sharf, "Adaptive reactionless motion for space manipulator when capturing an unknown tumbling target," *IEEE International Conference on Robotics and Automation*, 2011, pp. 4202-4207.

[14]K. Yoshida, R. Kurazumeand Y. Umetani, "Dual arm coordination in space free-flying robot," *IEEE International Conference on Robotics and Automation*, 1991, pp. 2516-2521.

[15]S. K. Agrawal and S. Shirumalla, "Planning motions of a dual-arm free-floating manipulator keeping the base inertially fixed," *Mechanism and Machine Theory*, vol. 30, no. 1, pp. 59-70, 1995.

[16]A. Ejiri, I. Watanabe, K. Okabayashi, M. Hashima, M. Tatewaki, T. Aoki, and T. Maruyama, “Satellite berthing experiment with a two-armed space robot,” *IEEE International Conference on Robotics and Automation*,1994,pp. 3480-3487.

[17]T. Miyabe, A. Konno, and M. Uchiyama, “Automated object capturing with a two-arm flexible manipulator,” *IEEE International Conference on Robotics and Automation*, 2003, pp. 2529-2534.

[18]R. Takahashi, H. Ise, A. Konno, M. Uchiyama and D. Sato, “Hybrid simulation of a dual-arm space robot colliding with a floating object,” *IEEE International Conference on Robotics and Automation*, 2008, pp. 1201-1206.

[19]W. Xu, Y. Liu, and Y.Xu, “The coordinated motion planning of a dual-arm space robot for target capturing,” *Robotica*, vol. 30, no. 5, pp. 755-771, 2012.

[20]Y. Umetani and K. Yoshida, “Resolved motion rate control of space manipulators with generalized jacobian matrix,” *IEEE Transactions on Robotics and Automation*, vol. 5, no. 3, pp. 303-314, 1989.

[21]S. V. Shah, P. V. Nandhial and S. K. Saha, “Recursive Dynamics Simulator (ReDySim)-A Multibody Dynamics Solver,” *Theoretical and Applied Mechanics Letters*, 2(6),pp. 063011:1-6, 2012.

[22]L. Righetti, M. Mistry, J. Buchli and S. Schaal, “Inverse dynamics control of floating-base robots with external constraints: an unified view,” *IEEE International Conference on Robotics and Automation*, pp. 1085-1090, 2011.

[23]E. Papadopoulos and S. Dubowsky, “Dynamic singularities in free-floating space manipulators,” *Journal of Dynamic Systems, Measurement and Control*, vol. 115, no. 1, pp. 44-52, 1993.

[24]N. Mansard, “A Dedicated Solver for Fast Operational-Space Inverse Dynamics,” *IEEE International Conference on Robotics and Automation*, pp. 4943-4949, 2012.

[25]A. Dietrich, T. Wimböck, H. Täubig, A. Albu-Schäffer, and G. Hirzinger, “Extensions to Reactive Self-Collision Avoidance for Torque and Position Controlled Humanoids,” *IEEE International Conference on Robotics and Automation*, pp. 3456-3462, 2011.